

Two-Dimensional Hybrid Dion–Jacobson Germanium Halide Perovskites

Congcong Chen, Xin Zhao, Yaping Gong, Yang Liu, Zhongwei Chen, Luming Zhang, Jian Chen, Zeyu Deng, Haipeng Lu, Min Luo, Pieremanuele Canepa,* and Lingling Mao*



Cite This: <https://doi.org/10.1021/acs.chemmater.3c00278>



Read Online

ACCESS |



Metrics & More

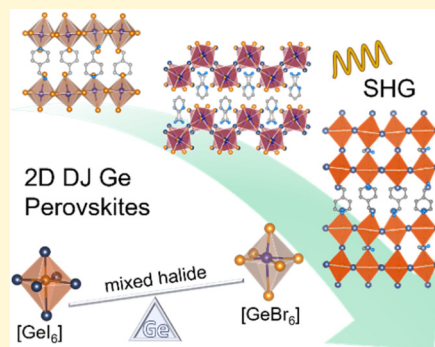


Article Recommendations



Supporting Information

ABSTRACT: Hybrid two-dimensional (2D) halide perovskites have emerged as an important class of high-performance semiconductors because of their excellent physical properties and structural diversity. Here, we report a new family of hybrid 2D Ge-based perovskites that have the Dion–Jacobson structure type, with the general formula $A(\text{MA})_{n-1}\text{Ge}_n\text{X}_{3n+1}$, where $A = 2$ -(aminomethyl)pyridinium (2AMPY), 3-(aminomethyl)pyridinium (3AMPY), 4-(aminomethyl)pyridinium (4AMPY), or 4-(aminomethyl)piperidinium (4AMP), $X = \text{Br}$ or I , and $n = 1$ or 2 . Single-crystal X-ray diffraction shows that most of the bromide structures are centrosymmetric, whereas the iodide analogues are all non-centrosymmetric. The optical band gaps are effectively regulated by the level of octahedral distortion of the corresponding $[\text{GeX}_6]$, where a larger distortion corresponds to a larger band gap. These compounds exhibit relatively weak photoluminescence, which can be observed at low temperatures. All of the Ge-based iodide perovskites exhibit good second-harmonic generation (SHG) responses, with the highest reaching $0.53 \times \text{AgGaS}_2$ for (4AMPY) GeI_4 , where their particle-dependent SHG has been investigated. First-principles calculations of the SHG properties are in good agreement with the experimental results. Furthermore, layer transformation can be achieved from the (100)- to (110)-oriented configuration by mixing the halides, which is a rare example. These results showcase the versatility and diversity of employing an asymmetric dication and the Ge^{2+} metal to achieve SHG active non-centrosymmetric materials, providing new strategies for the design of lead-free alternatives with interesting photophysical properties.



INTRODUCTION

Hybrid organic–inorganic halide perovskites are remarkable semiconductors that have a wide range of optoelectronic applications such as solar cells,^{1–4} light-emitting diodes (LEDs),^{5–7} photodetectors,^{8–10} and lasers.^{11–13} The most extensively studied three-dimensional (3D) perovskites are defined by the general AMX_3 formula, where A is a small cation [Cs^+ , CH_3NH_3^+ (MA), and $\text{HC}(\text{NH}_2)_2^+$ (FA)], M is a metal cation (Ge, Sn, or Pb), and X is a halide anion (Cl^- , Br^- , or I^-).¹⁴ The ideal cubic structure of corner-sharing octahedral $[\text{MX}_6]$ units of 3D perovskite is limited to a range of compositions, constrained by the Goldschmidt tolerance factor.¹⁵ The possibility of dimensional reduction, for example, when larger organic spacer cations are inserted, cleaves the 3D structure into (100), (110), and (111) crystallographic planes.¹⁶ The obtained two-dimensional (2D) perovskites, by contrast, not only exhibit improved stability but also provide more chemically diverse structures and tunable physical properties, improving the photovoltaic efficiency¹⁷ and leading to advancements in LEDs.¹⁸

So far, there are two main categories of (100)-oriented 2D halide perovskites reported, namely, Ruddlesden–Popper (RP) phases^{19–21} and Dion–Jacobson (DJ) phases.^{22–26} The alternating cations in the interlayer space (ACI) types have

also been reported, but with fewer examples.^{27,28} The differences between these types originate from the choice of spacing organic/inorganic cations, with relatively different stacking of the layers.^{19,22,28} The general formulas for the RP and DJ phases are $A'_2A_{n-1}M_nX_{3n+1}$ and $A'A_{n-1}M_nX_{3n+1}$, respectively, where the larger spacing cation A' is monovalent (+1) for the RP phases and divalent (+2) for the DJ phases. The RP phases contain monovalent cations interdigitated between the adjacent inorganic layers, and the continuous inorganic layers are shifted with respect to each other by a half-unit cell.^{19,23} In the case of DJ phases, they consist of short divalent spacer cations between the layers, and the inorganic layers stack exactly on top of each other. Compared with the RP phases, the DJ phases with a single layer of dications feature a shorter interlayer distance that enhances the electronic coupling and charge transport between the inorganic layers.^{29,30}

Received: February 7, 2023

Revised: March 25, 2023

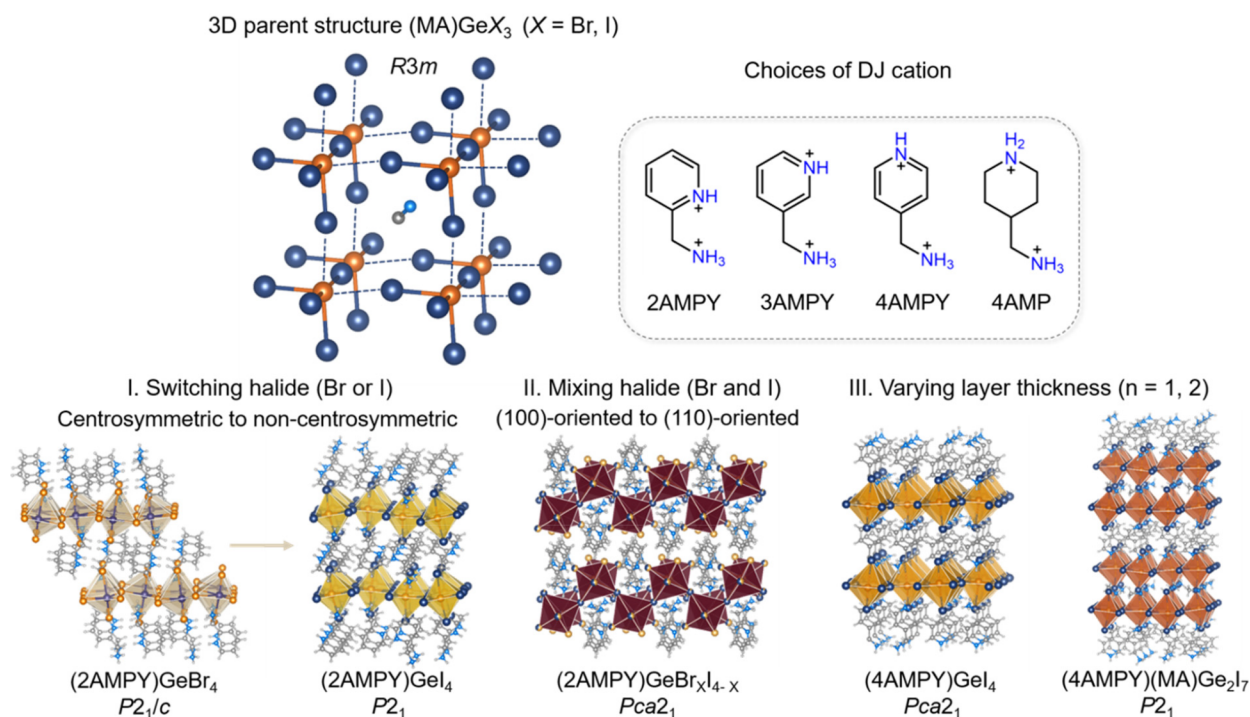


Figure 1. Crystal structure of a 3D (MA)GeX₃ (X = Br or I) structure with three short bonds and three long bonds (top left). Structures of cations 2AMPY, 3AMPY, 4AMPY, and 4AMP (top right). Schematic representation of the regulation of structural types in the 2D perovskite family (bottom).

However, the reports on 2D DJ hybrid perovskites have mainly been focused on the Pb-based phases,^{22–26} which limit the further structural exploration and understanding of the physical properties. Within the same group of elements, Ge has obvious advantages with a sterically active 4s² lone pair and strong off-centering resulting from the smaller ionic radius for the halide system.^{31–33} This results in a much higher probability of generating non-centrosymmetric structures and large polarizations, as seen in the 3D parent phase (MA)GeX₃ (Figure 1, top left).^{31,32} The first hybrid layered Ge-based perovskite (C₄H₉NH₃)GeI₄ was reported by Mitzi in 1996, who illuminated its crystal structure and optical properties.³⁴ Currently, examples of 2D Ge-based perovskites are still rare, mainly on RP phases,^{35,36} which have prompted us to investigate 2D DJ perovskites with new photophysical properties.^{35–38}

Here, we report the synthesis, structural analysis, and optical and nonlinear optical properties of 13 new 2D Ge perovskites using an array of similar asymmetric organic dications. Among these new phases, most of the bromide structures are centrosymmetric, whereas the iodide analogues are all non-centrosymmetric (Figure 1, bottom I). We have found that even though the bromide and iodide phases are both regular (100)-oriented DJ types, the mixing of Br and I results in changes in the layer orientation, giving rise to three series of (110)-oriented corrugated structures, regardless of the organic cation (Figure 1, bottom II). Further structural tunability has been demonstrated via the variation of layer thickness in this family (Figure 1, bottom III). The optical band gaps of these phases are highly tunable, and the photoluminescence (PL) emission can be observed at low temperatures. These materials exhibit good second-harmonic generation (SHG) responses, and they can be correlated with individual structural features. Density functional theory (DFT) reveals impressive SHG

characteristics of the Ge-based DJ iodide materials. Our work provides new design strategies for the synthesis of and tailoring of the properties of new 2D Ge-based halide materials, laying the foundation for the advancement of next-generation optoelectronics.

RESULTS AND DISCUSSION

Crystal Structure Analysis. The new DJ phases reported here are synthesized via a solution method, where GeO₂ and cations [2-(aminomethyl)pyridinium (2AMPY), 3-(aminomethyl)pyridinium (3AMPY), 4-(aminomethyl)pyridinium (4AMPY), 4-(aminomethyl)piperidinium (4AMP), or MA] are dissolved in a concentrated aqueous acid (HBr or HI) and H₃PO₂ (reducing agent) under stirring and heated to a boil. The single crystals are obtained by slow cooling at room temperature without perturbation. The optical microscopic pictures of single crystals are shown in Figure 2. The plate-like single crystals exhibit typical layered morphologies, except for (2AMPY)GeI₄ crystals that are elongated plates (Figure 2). Visualizations of the offsets of these structures are shown in Figures S6 and S7. For (4AMP)GeBr₄, (2AMPY)GeI₄, (4AMPY)GeI₄, (3AMPY)(MA)Ge₂I₇, and (4AMPY)(MA)Ge₂I₇, the layers can stack in a perfect (0, 0) displacement arrangement. For the other perovskites, the layered structures have slight offsets, and (2AMPY)GeBr₄ shows the largest displacement. Detailed crystallographic data and structural refinements for all compounds reported here are listed in Tables S1–S17. For the Ge-based DJ bromide perovskites, single-crystal X-ray diffraction shows that the symmetry of the four crystal structure ranges from monoclinic to orthorhombic, where (2AMPY)GeBr₄ and (3AMPY)GeBr₄ crystallize in space group *P2₁/c*, and (4AMPY)GeBr₄ and (4AMP)GeBr₄ crystallize in space groups *Pbca* and *Pmn2₁*, respectively. Interestingly, only (4AMP)GeBr₄ crystallizes in a

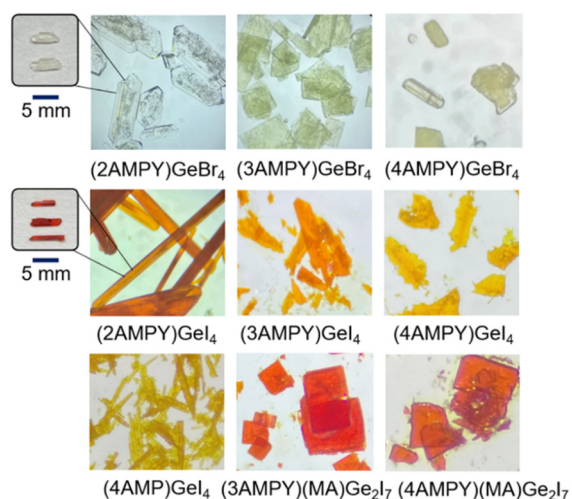


Figure 2. Optical microscopic pictures of Ge-based DJ perovskite single crystals. Crystal sizes range from 2 to 5 mm.

non-centrosymmetric space group. These compounds belong to the (100)-oriented 2D structural type, composed of corner-sharing $[\text{GeBr}_6]$ octahedral layers with the nonsymmetrical dications sandwiched between them (Figure 3a–d). In the 3D parent structure (MA)GeBr₃, the short and long bonds are oriented in the same way, and each Br atom is coordinated with both a short bond and a long bond (Figure 1, top left). However, the Ge-based DJ bromide perovskites have different arrangements, such as (2AMPY)GeBr₄, in which each apical atom is attached to the Ge by a long bond, and the long bond is in opposite directions for Ge1 and Ge2 (Figures S1 and S2). In Figure S2, it is clear that the lone pairs are sitting in the same positions for (2AMPY)GeBr₄, (3AMPY)GeBr₄, and (4AMPY)GeBr₄, where they are all centrosymmetric. For

(4AMPY)GeBr₄, the lone pairs are on a wave-like orientation, possibly resulting in its non-centrosymmetric structure. We also observe that the inorganic layers are obviously offset especially for (2AMPY)GeBr₄, which is possibly related to the *ortho*-position of the NH⁺ group. Because the optical and electronic properties are heavily influenced by the individual distortion level of the $[\text{GeBr}_6]$ octahedron, the distortion levels of the octahedra themselves can be quantified by defining the distortion index (D) and their bond angle variance (σ^2) based on Ge–X bond lengths and Ge–X–Ge bond angles calculated using VESTA.^{39,40} The average D of the entire collection and average σ^2 values of different $[\text{GeX}_6]$ octahedra are listed in Table 1 (X = Br or I). From these data, we can see that the

Table 1. Summary of Average Ge–X–Ge Angles, Bond Length Distortion Indices (D_{avg}), Bond Angle Variance (σ^2_{avg}), and Optical Band Gaps for the Compounds Reported Here in Comparison with the 3D Phases^{31,32, a}

| compound | average Ge–X–Ge angle (deg) | D_{avg} | σ^2_{avg} | band gap (eV) |
|---|-----------------------------|------------------|-------------------------|---------------|
| (2AMPY)GeBr ₄ | 160.36 | 0.16 | 84.88 | 3.14 |
| (3AMPY)GeBr ₄ | 169.83 | 0.13 | 40.79 | 2.87 |
| (4AMPY)GeBr ₄ | 172.88 | 0.13 | 50.52 | 2.93 |
| (4AMPY)GeBr ₄ | 166.59 | 0.14 | 85.06 | 3.27 |
| (2AMPY)GeI ₄ | 168.67 | 0.08 | 37.53 | 2.28 |
| (3AMPY)GeI ₄ | 167.88 | 0.08 | 36.63 | 2.25 (2.78) |
| (4AMPY)GeI ₄ | 158.76 | 0.05 | 31.19 | 2.28 (2.61) |
| (4AMPY)GeI ₄ | 161.68 | 0.11 | 58.07 | 2.32 |
| (3AMPY)(MA)Ge ₂ I ₇ | 168.58 | 0.10 | 37.32 | 2.14 (2.99) |
| (4AMPY)(MA)Ge ₂ I ₇ | 168.44 | 0.10 | 43.67 | 2.17 (2.92) |
| (MA)GeBr ₃ | 170.59 | 0.14 | 24.69 | 2.91 |
| (MA)GeI ₃ | 167.66 | 0.11 | 44.88 | 1.96 |

^aComputed band gaps of selected materials at the PBE0 level of theory in parentheses.

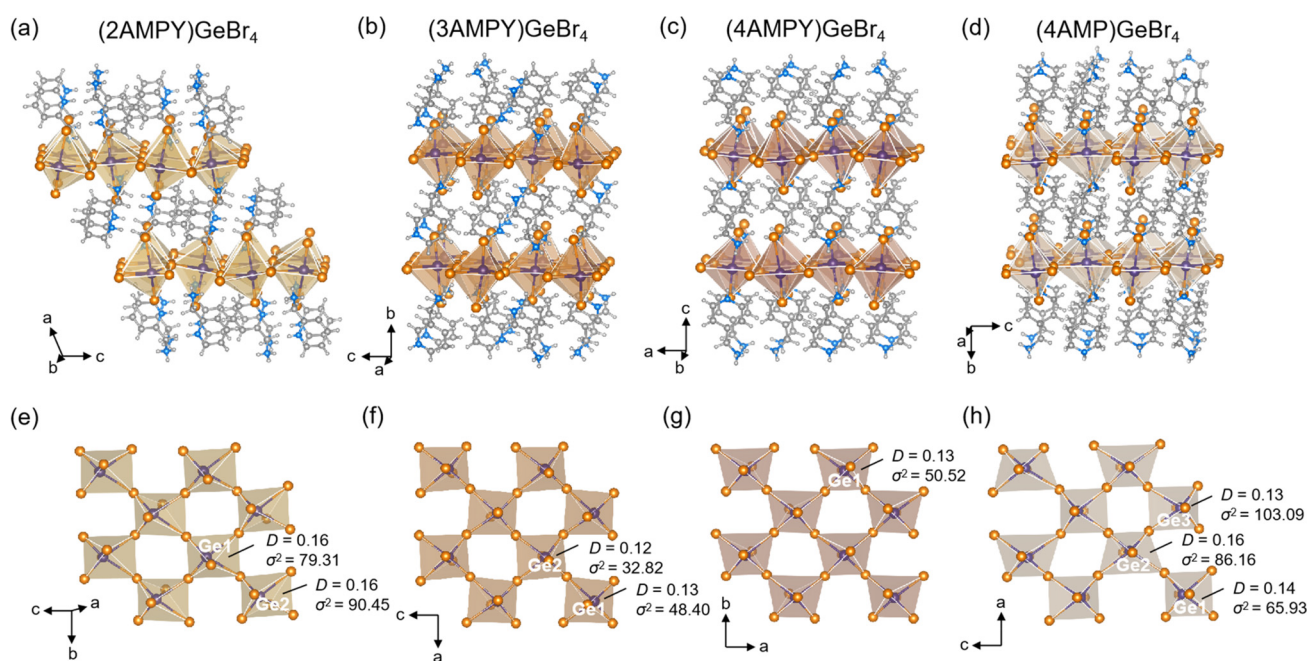


Figure 3. Crystal structure and inorganic layer of the corner-sharing $[\text{GeBr}_6]$ octahedron for (a and e) (2AMPY)GeBr₄, (b and f) (3AMPY)GeBr₄, (c and g) (4AMPY)GeBr₄, and (d and h) (4AMPY)GeBr₄. Color scheme for the atoms: navy (Ge), orange (Br), blue (N), gray (C) and light gray (H).

distortion of $[\text{GeBr}_6]$ octahedra is highly relevant to the choice of cation (Figure 3e,f), where the average distortions of $(2\text{AMPY})\text{GeBr}_4$ and $(4\text{AMP})\text{GeBr}_4$ are larger than those of $(3\text{AMPY})\text{GeBr}_4$ and $(4\text{AMPY})\text{GeBr}_4$. The Ge–Br–Ge angles also decrease with the degree of octahedral distortion. In particular, $(2\text{AMPY})\text{GeBr}_4$ has a very pronounced octahedral distortion, which may be caused by the greater octahedral tilting effect of the asymmetric arrangement of the NH_3^+ groups in the aromatic diammonium ions compared to those of $(3\text{AMPY})\text{GeBr}_4$ and $(4\text{AMPY})\text{GeBr}_4$.

All of the Ge-based DJ iodide perovskites crystallize in non-centrosymmetric space groups. The variations of bond length and angle are less dramatic compared with those of the bromide analogues (see Figure 4). The negative charge on the

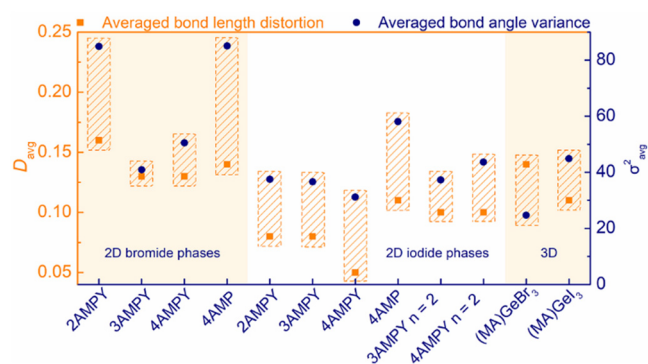


Figure 4. Summary of the averaged bond length distortion (D_{avg}) and bond angle variance (σ_{avg}^2) for 2D and 3D Ge-based perovskites.

iodide atom is more delocalized due to its larger ionic radius, which may weaken the relative strength of hydrogen bonds, resulting in less distorted structures.⁴¹ However, the symmetry of these phases is not directly related to the distortion levels. The iodide phases are all non-centrosymmetric, likely due to the higher level of lone pair expression of the small Ge cation paired with the larger iodide anion. With respect to the distortion of $[\text{GeI}_6]$ octahedra, $(4\text{AMP})\text{GeI}_4$ exhibits the largest bond length distortion and bond angle variance among these single-layer perovskites ($n = 1$). The distortion level ($D_{\text{avg}} = 0.02$; $\sigma_{\text{avg}}^2 = 9.47$) for the Pb analogue $(4\text{AMP})\text{PbI}_4$ is much smaller than that of $(4\text{AMP})\text{GeI}_4$. It seems to be universal that Ge-based phases have larger distortions compared with those of the Pb analogues for both 2D and 3D perovskites. It is worth noting that there are two kinds of Ge–I bonds (short and long bond) in the $[\text{GeI}_6]$ octahedra because of the prominent lone pair effect of Ge^{2+} . For example, the bond length in $(4\text{AMPY})\text{GeI}_4$ ranges from 2.73 Å (short bond) to 3.47 Å (long bond) (Figure 5a), and the I–Ge–I bond angles significantly deviate from 90°. We select two pairs of ($n = 1$ and 2), namely, $(3\text{AMPY})\text{GeI}_4$, $(4\text{AMPY})\text{GeI}_4$, $(3\text{AMPY})(\text{MA})\text{Ge}_2\text{I}_7$, and $(4\text{AMPY})(\text{MA})\text{Ge}_2\text{I}_7$, as representative examples to illustrate the structural nuances. For the $n = 1$ phases, the layers are stacking on top of each other viewed from the top, where $(4\text{AMPY})\text{GeI}_4$ mainly has in-plane distortion and $(3\text{AMPY})\text{GeI}_4$ exhibits out-of-plane tilting (Figure S5). The difference in the organic cation has a great effect on the Ge–I–Ge angles, which is related to the optical properties (more details will be discussed in the next section). As shown in panels b and c of Figure 5, the inorganic layer of $(4\text{AMPY})\text{GeI}_4$ has a larger distortion compared with $(3\text{AMPY})\text{GeI}_4$, where the average Ge–I–Ge angle is

158.76° for $(4\text{AMPY})\text{GeI}_4$ and 167.9° for $(3\text{AMPY})\text{GeI}_4$. These angles are larger than those of the Pb-based analogues [149.2° for $(4\text{AMPY})\text{PbI}_4$ and 166.3° for $(3\text{AMPY})\text{PbI}_4$].²³ As the layer number increases to $n = 2$, the averaged Ge–I–Ge angle increases to 168.4° for 4AMPY and 168.6° for 3AMPY, suggesting that the influence of the organic spacer is reduced as the inorganic layer becomes thicker. However, the degree of individual octahedral distortion (D and σ^2) increases (Figure 5f). Another fascinating structural feature is that the interlayer distance between inorganic layers is relatively short. For the 4AMPY series, the interlayer distance is 3.85 Å for the $n = 2$ sample (Figure 5d), shorter than that in the $n = 1$ sample. The inorganic slab thickness is 3 times the interlayer distance (12.10 Å). The long and short Ge–I bonds (~ 2.7 and 3.4 Å) exist in the 2D phases (both $n = 1$ and 2 in Figure 5a,e) and 3D parent structure $(\text{MA})\text{GeI}_3$. This suggests the Ge–I units are rather disconnected due to the presence of three short and three long bonds within the $[\text{GeI}_6]$ octahedron. On the contrary, the individual octahedral distortion is smaller for the 2D $n = 2$ phases (see Table 1), showing the lone pair expression in $n = 2$ is less pronounced than that of the 3D phases.³¹

Optical Properties. The structural differences in these DJ layered phases further influence the optical properties. The optical absorption spectra were recorded via diffuse reflectance spectroscopy, and the raw data were converted using the Kubelka–Munk function.⁴² These materials all exhibit obvious exciton peaks near the absorption edge, because of the quantum confinement effects. The optical band gap of these DJ perovskites can be effectively regulated by the choice of organic spacer. For the bromide phases (Figure 6a), the optical band gap is 3.14 eV for $(2\text{AMPY})\text{GeBr}_4$, 2.87 eV for $(3\text{AMPY})\text{GeBr}_4$, 2.93 eV for $(4\text{AMPY})\text{GeBr}_4$, and 3.27 eV for $(4\text{AMP})\text{GeBr}_4$, which is consistent with the color of these materials (Figure 2). Unlike the Pb-based perovskites, where a rather large band gap difference is usually expected between the 2D $n = 1$ and 3D phases, the band edges for the 2D and 3D Ge-based bromide perovskites are much closer and even overlap for $(3\text{AMPY})\text{GeBr}_4$ and $(\text{MA})\text{GeBr}_3$ (as shown in Figure 6a). Although usually the M–X–M angles play an important role in determining the band gap, for the Ge-based phases it is more significant to compare the octahedral distortion on the basis of the distortion levels, to further comprehend the structure–property relationship. The band gap evolution is consistent with the average bond angle variance (σ_{avg}^2) (Table 1), where greater distortion obviously leads to a larger band gap. Within the iodide phases, these analogues have narrower band gaps (Figure 6b), consistent with what is usually observed in the Pb- or Sn-based phases. $(4\text{AMP})\text{GeI}_4$ has an absorption edge at 2.32 eV, which is the highest among the 2D $n = 1$ Ge-based perovskites, while other compounds ($n = 1$) have relatively similar band gaps [2.28 eV for $(2\text{AMPY})\text{GeI}_4$, 2.25 eV for $(3\text{AMPY})\text{GeI}_4$, and 2.28 eV for $(4\text{AMPY})\text{GeI}_4$]. This is clearly related to the average bond angle variance (σ_{avg}^2), as the σ_{avg}^2 for $(4\text{AMP})\text{GeI}_4$ is significantly higher than those of the other compounds. As the layer number increases to $n = 2$, the band gap for $(3\text{AMPY})(\text{MA})\text{Ge}_2\text{I}_7$ decreases slightly from 2.25 to 2.14 eV, whereas for $(4\text{AMPY})(\text{MA})\text{Ge}_2\text{I}_7$, it decreases from 2.28 to 2.17 eV. Here, the differences of the absorption edges are very small (~ 0.1 eV) between $n = 1$ and 2. Fundamental band gaps predicted by the hybrid DFT (PBE0) of Table 1 overestimate the measured values. We observe that their band gap variations

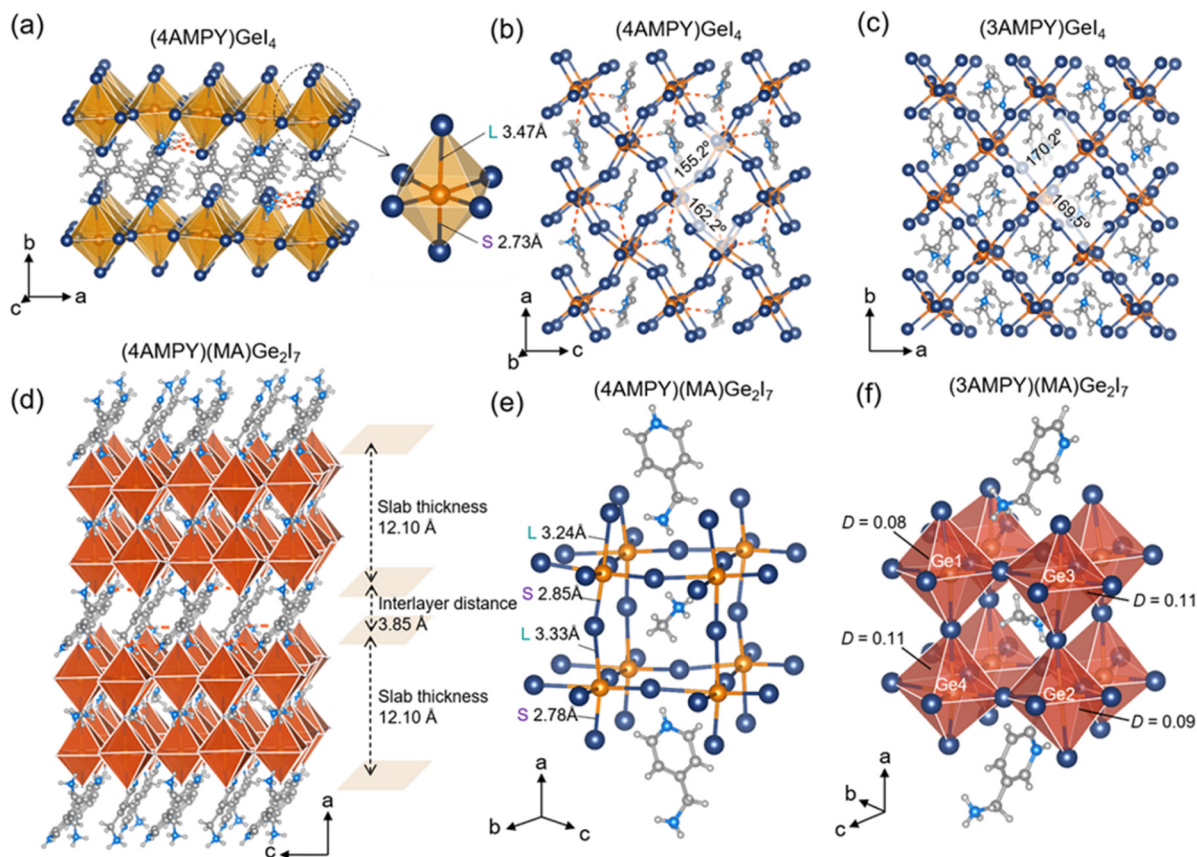


Figure 5. (a) Crystal structure of $(4\text{AMPY})\text{GeI}_4$ and the individual $[\text{Ge}_6]$ octahedron. Structural comparison of (b) $(4\text{AMPY})\text{GeI}_4$ and (c) $(3\text{AMPY})\text{GeI}_4$. (d) Crystal structure of $(4\text{AMPY})(\text{MA})\text{Ge}_2\text{I}_7$. Structural comparison of (e) $(4\text{AMPY})\text{GeI}_4$ and (f) $(3\text{AMPY})\text{GeI}_4$. The hydrogen bonds are marked with orange dashed lines (H-bond cutoff of 3.50 Å). Color scheme for the atoms: orange for Ge, navy for I, blue for N, gray for C, and light gray for H.

are not as pronounced compared with those of the Pb-based iodide phases.²³

Because the Ge-based perovskites are typically not very emissive,³¹ steady-state PL measurements for these compounds were performed at 80 K (Figure 7a). These Ge-based 2D phases exhibit weak PL in general, similar to previous observations.^{32,36} The emission centers of the PL emission for $(2\text{AMPY})\text{GeBr}_4$ (438 nm, 2.83 eV), $(3\text{AMPY})\text{GeBr}_4$ (456 nm, 2.73 eV), and $(4\text{AMPY})\text{GeBr}_4$ (446 nm, 2.78 eV) are relatively close together, under 285, 255, and 280 nm excitation, respectively. These PL peaks are relatively narrow and close to the band edge, which belong to free exciton (FE) emission. These signatures are similar to those of the reported 2D Ge-based bromide perovskites.³⁷ For the iodide phases, we can observe weak and broad PL emission peaks at 755 nm for $(3\text{AMPY})\text{GeI}_4$ ($n = 1$) and 735 nm for $(3\text{AMPY})(\text{MA})\text{Ge}_2\text{I}_7$ ($n = 2$), with full widths at half-maximum (fwhms) of 227 and 220 nm, respectively. The corresponding large Stokes shifts (350 nm for $n = 1$ and 330 nm for $n = 2$) are due to the strong electron–phonon coupling in such a distorted structure.⁴³ Such broad PL peaks are commonly observed in Ge-based halide perovskites;^{32,36} the origin of the broad emission could be due to the existence of self-trapped excitons resulting from transient structural defect states.^{44,45} As the temperature increases, the PL intensities of $(3\text{AMPY})\text{GeI}_4$ ($n = 1$) and $(3\text{AMPY})(\text{MA})\text{Ge}_2\text{I}_7$ ($n = 2$) weaken and become negligible at room temperature (Figure 7b,c), which is usually induced by thermal quenching.

Structural Transformation with Halide Mixing. The synthesis of a solid solution at the halide site plays a crucial role in modulating the crystal structure and also provides a facile method for regulating the optical properties. Typically for 2D and 3D perovskites, mixing the halides will lead to solid solutions without changing the structure significantly.^{46,47} However, we have found $(2\text{AMPY})\text{GeBr}_4$ originally featuring conventional (100)-oriented 2D structure can be transformed into a new structural type with a (110)-oriented configuration when mixed with iodine (Figure 8a). Moreover, the corresponding space group is also changed from centrosymmetric space group $P2_1/c$ to non-centrosymmetric space group $Pca2_1$ for the case of $(2\text{AMPY})\text{GeBr}_x\text{I}_{4-x}$ (x is refined as 0.5–1.6 in the refinement), with a detectable SHG signal at room temperature (Figure S18). Within the 3AMPY and 4AMPY series, the structural changes to a (110)-oriented type after mixing are similar to the case of 2AMPY, whereas the space groups of the structures are centrosymmetric $Pbcm$. Here, we have selected $(2\text{AMPY})\text{GeBr}_x\text{I}_{4-x}$ series as an example to discuss the details. The layered morphology of the mixed halide perovskites can be observed by scanning electron microscopy (SEM), as shown in Figure S15. Chemical analyses of these crystals were performed by energy dispersive spectroscopy (EDS), in which the actual obtained Br:I atomic ratio is 1.6:2.4 (when the experimental input of the HBr:HI ratio is 7:1), which slightly deviated from the Br:I ratio of 2.1:1.9 refined by single-crystal XRD. The macroscopic distribution of Br and I should be roughly close to the EDS

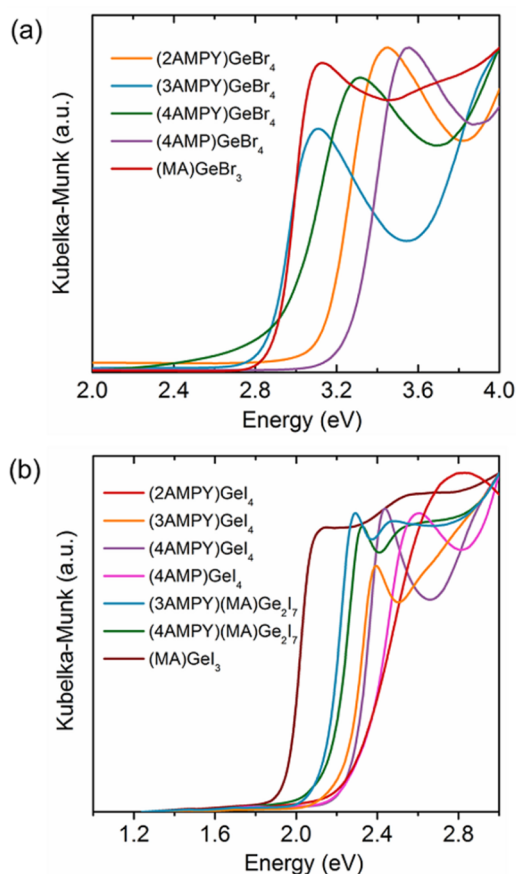


Figure 6. Optical absorption spectra of (a) Ge-based DJ bromide compounds and (b) Ge-based DJ iodides.

analysis (see Table S18). From Figure 8b, it is evident that for the $(2\text{AMPY})\text{GeBr}_x\text{I}_{4-x}$ series when $x = 0.5, 1,$ and 1.6 , they all belong to the new (110) -oriented phase, matching the simulated pattern for the $x = 1.6$ member. The 2θ angle with an increasing I content (decreasing x) is shifting to the smaller angle, indicating unit cell expansion, which is expected as the ionic radius of I^- is larger than that of Br^- . The trend of optical absorption is quite interesting as shown in Figure 8c, and the mixed $(2\text{AMPY})\text{GeBr}_x\text{I}_{4-x}$ series ($x = 0.5, 1,$ and 1.6) members all have absorption edges close to or below that of $(2\text{AMPY})\text{GeI}_4$ (~ 2.3 eV), which certainly are far lower than that of the Br end member (~ 3.1 eV). These results suggest

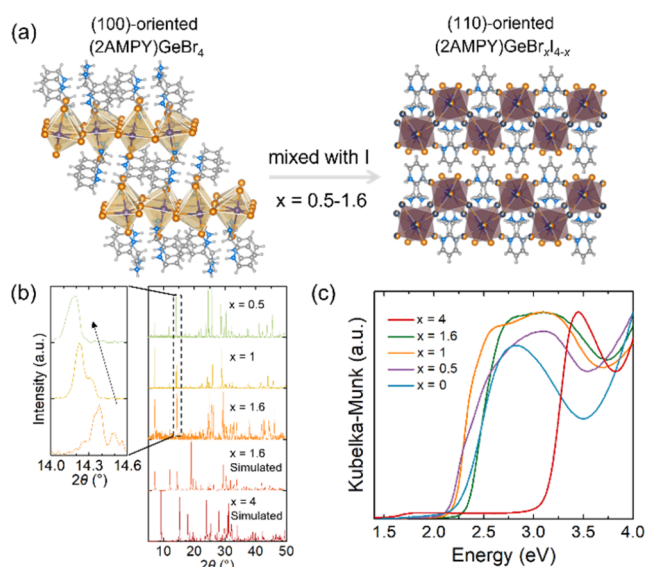


Figure 8. (a) Illustration of the structural changes when mixing with I at the Br position. (b) Resulting powder XRD patterns and (c) optical absorption spectra of the $(2\text{AMPY})\text{GeBr}_x\text{I}_{4-x}$ ($0 \leq x \leq 4$) series.

with the flexible handle of halide mixing, the structures and properties can be effectively tuned.

Second-Harmonic Generation Responses. A prerequisite for the SHG response is for the crystal structure to be non-centrosymmetric.⁴⁸ The non-centrosymmetric feature of the Ge-based iodine phases described above prompts us to measure their SHG properties. The polycrystalline powder SHG responses were measured under 1064 nm laser irradiation using potassium dihydrogen phosphate (KDP) as a reference at room temperature. All of these compounds show efficient SHG signals at particle sizes of 70–100 μm (Figure 9a and Figure S18). The SHG intensities of these compounds are $\sim 0.62, \sim 0.60, \sim 0.71,$ and ~ 0.55 times that of KDP for $(3\text{AMPY})\text{GeI}_4, (4\text{AMPY})\text{GeI}_4, (3\text{AMPY})(\text{MA})\text{Ge}_2\text{I}_7,$ and $(4\text{AMPY})(\text{MA})\text{Ge}_2\text{I}_7,$ respectively. The SHG intensity of $(4\text{AMPY})\text{GeI}_4$ is the weakest among the (100) -oriented perovskites reported here ($0.15 \times \text{KDP}$), which is likely due to it having the largest band gap among the group. Changing the structural type by mixing the halides weakens the SHG intensity of the obtained (110) -oriented perovskites compared with that of $(2\text{AMPY})\text{GeI}_4$ (Figure S18 and Table S19). Note that the optical band gaps of these compounds are in the range

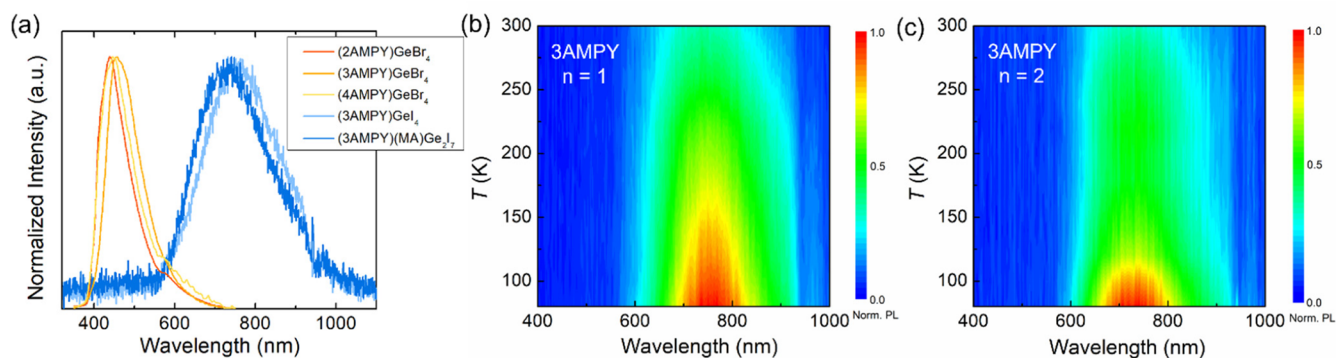


Figure 7. (a) PL emission spectra of $(2\text{AMPY})\text{GeBr}_4, (3\text{AMPY})\text{GeBr}_4, (4\text{AMPY})\text{GeBr}_4, (3\text{AMPY})\text{GeI}_4,$ and $(3\text{AMPY})(\text{MA})\text{Ge}_2\text{I}_7$ at 80 K. 2D pseudocolor plot of the normalized emission spectra for (b) $(3\text{AMPY})\text{GeI}_4$ ($n = 1$) and (c) $(3\text{AMPY})(\text{MA})\text{Ge}_2\text{I}_7$ ($n = 2$) from 80 to 300 K.

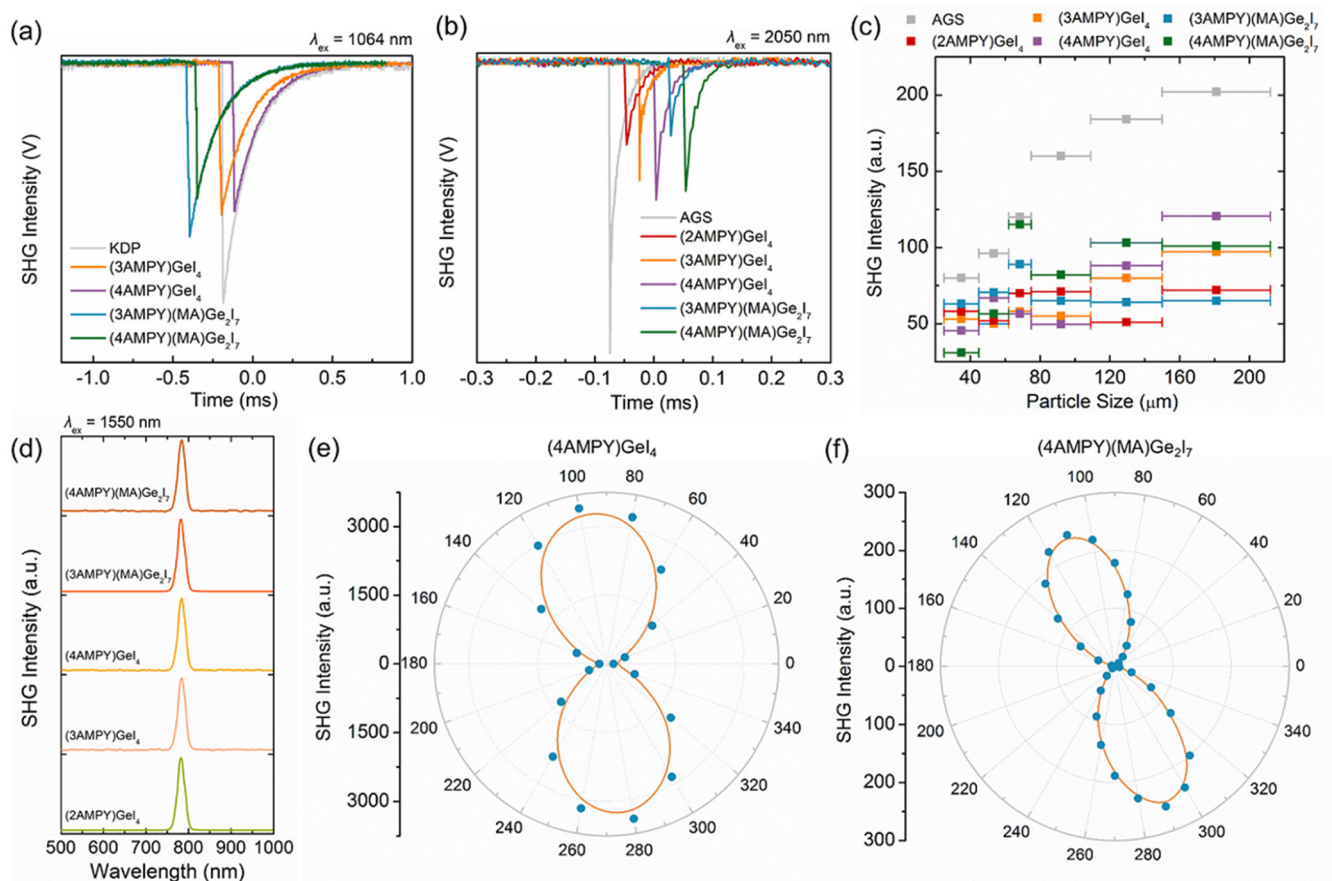


Figure 9. Nonlinear optical properties of a series of non-centrosymmetric compounds. (a) SHG signals of x AMPY ($x = 3$ and 4) series in the particle size range ($70\text{--}100\ \mu\text{m}$) at room temperature and compared with KDP. (b) SHG intensity of x AMPY ($x = 2, 3,$ and 4) series in the particle size range ($150\text{--}212\ \mu\text{m}$) at room temperature and compared with AGS. (c) SHG intensity of x AMPY ($x = 2, 3,$ and 4) series and AGS with different particle sizes at room temperature. (d) SHG spectra of representative compounds under $1550\ \text{nm}$ laser irradiation. Polar SHG intensity plots of (e) $(4\text{AMPY})\text{GeI}_4$ and (f) $(4\text{AMPY})(\text{MA})\text{Ge}_2\text{I}_7$ as a function of polarization angle under $1550\ \text{nm}$ laser irradiation.

of $2.14\text{--}2.32\ \text{eV}$ below $\lambda/2 = 532\ \text{nm}$ ($2.33\ \text{eV}$); the obtained SHG intensity would be theoretically low considering the effect of linear absorption.³¹ To avoid the absorption that potentially lowers the SHG, we select several compounds with relatively strong SHG signals for further measurements under $2050\ \text{nm}$ laser irradiation, using AgGaS_2 (AGS) as the reference at room temperature (Figure 9b). These compounds have relatively strong SHG responses in the particle size range of $150\text{--}212\ \mu\text{m}$, ~ 0.35 , ~ 0.47 , ~ 0.53 , ~ 0.33 , and ~ 0.50 times that of AGS for $(2\text{AMPY})\text{GeI}_4$, $(3\text{AMPY})\text{GeI}_4$, $(4\text{AMPY})\text{GeI}_4$, $(3\text{AMPY})(\text{MA})\text{Ge}_2\text{I}_7$, and $(4\text{AMPY})(\text{MA})\text{Ge}_2\text{I}_7$, respectively. In particular, the SHG signals of $n = 1$ phases are slightly stronger than those of $n = 2$ phases, which does not increase with layer thickness (which is closer to the 3D structure), as previously reported.¹⁹ This phenomenon may be related to the degree of octahedral distortion, as the 4AMPY series ($n = 1$ and 2) exhibit the strongest SHG response in the largest particle size range ($150\text{--}212\ \mu\text{m}$). As illustrated in Figure 9c, the SHG intensity of these compounds fluctuates with an increase in particle size (non-phase-matchable). The SHG properties of the single crystals were further characterized using a microscope with a $1550\ \text{nm}$ laser. The frequency-doubled signals are centered at half the pumping wavelength ($775\ \text{nm}$), consistent with the expected SHG signals (Figure 9d). These Ge-based materials have much stronger SHG responses compared with those of the Pb-based

analogues.⁴⁹ We further study the anisotropy of the SHG response for $(4\text{AMPY})\text{GeI}_4$ and $(4\text{AMPY})(\text{MA})\text{Ge}_2\text{I}_7$ by tuning the $\lambda/2$ plate to measure its SHG intensity as a function of the polarization angle (Figure 9e,f). The obtained polar plot of the SHG signal embodies a dumbbell shape and exhibits different axisymmetric geometries. The SHG responses reach a maximum at polarization angles of 100° and 280° for $(4\text{AMPY})\text{GeI}_4$, while the maximum SHG responses emerge at 110° and 290° polarization for $(4\text{AMPY})(\text{MA})\text{Ge}_2\text{I}_7$. The SHG intensity gradually decreases, thus reaching minimum values with the rotation of the polarization direction. The SHG anisotropy ratio, quantized as $\rho = (I_{\text{max}} - I_{\text{min}})/(I_{\text{max}} + I_{\text{min}})$, where I_{max} and I_{min} correspond to the maximum and minimum values of SHG intensity, respectively, was determined to be $\sim 91.3\%$ and $\sim 99.9\%$ for $(4\text{AMPY})\text{GeI}_4$ and $(4\text{AMPY})(\text{MA})\text{Ge}_2\text{I}_7$, respectively, comparable to those of the reported chiral hybrid organic–inorganic halide perovskites.^{50–52} This suggests the SHG intensity is strongly related to the crystal symmetry and highly anisotropic.

First-Principles Calculations. Following our previous work,^{32,53} we performed all-electron first-principles calculations based on DFT as implemented in CRYSTAL17⁵⁴ to inspect the SHG of selected non-centrosymmetric 2D Ge-based compounds as a function of direction (Figure 10). Previously, we demonstrated the importance of using all-electron and hybrid functionals (in the flavor of PBE0-D3, including also

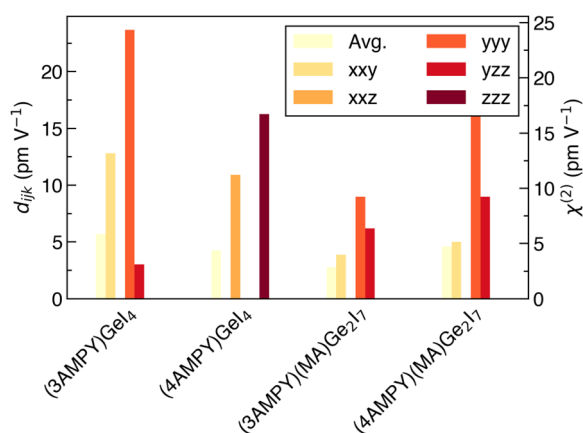


Figure 10. Computed direction-dependent values of the $\chi^{(2)}$ tensor of selected non-centrosymmetric 2D Ge-based materials. Avg. represents an arithmetic average of all directions. Note that the conversion between the $\chi_{ijk}^{(2)}$ and d_{ijk} components is $\chi_{ijk}^{(2)} = 2d_{ijk}$.

van der Waals correction) in the prediction of accurate second-harmonic response properties of hybrid organic–inorganic materials. The computational details of this study are similar to those of ref 33, and details of these calculations are given in the Supporting Information. Note that all structural models used in these predictions are significant in size (>150 atoms), which makes these hybrid DFT calculations extremely challenging. In general, a comparison of the largest values of $\chi^{(2)}$ predicted by the non-centrosymmetric 2D Ge-based compounds suggests $(3\text{AMPY})\text{GeI}_4 > (4\text{AMPY})\text{GeI}_4 > (4\text{AMPY})(\text{MA})\text{Ge}_2\text{I}_7 \gg (3\text{AMPY})(\text{MA})\text{Ge}_2\text{I}_7$, which appears in reasonable agreement with the experimental data. With the exception of $(4\text{AMPY})\text{GeI}_4$, the other 2D perovskites consistently show maxima of SHG activity [either $\chi^{(2)}$ or d_{ijk}] along the yyy direction, following the order for $\chi_{yyy}^{(2)}$ of $(3\text{AMPY})\text{GeI}_4 > (4\text{AMPY})(\text{MA})\text{Ge}_2\text{I}_7 \gg (3\text{AMPY})(\text{MA})\text{Ge}_2\text{I}_7$. The maximum value of $\chi_{yyy}^{(2)}$ ($\sim 23.68 \text{ pm V}^{-1}$) was found for $(3\text{AMPY})\text{GeI}_4$. Notably, the second-harmonic activity of all of these 2D Ge-based compounds is in most cases better than those of standard inorganic compounds, such as KDP [$\chi^{(2)} \sim 0.28 \text{ pm V}^{-1}$].³²

CONCLUSION

In conclusion, a structurally diverse series of new 2D Ge-based DJ halide perovskites can be successfully synthesized using the solution method with different organic templating dications. The non-centrosymmetric assembly of 2D Ge perovskites has been achieved in the iodide series by utilizing Ge^{2+} as the central metal with a smaller ionic radius compared with Pb and a sterically active lone pair. The features of the asymmetric organic spacer cations such as the protonation site and rigidity of the cation have a significant impact on the crystal structure, including the tilting of the octahedra and the stacking of inorganic layers, which result in differences in their corresponding optical properties. These 2D non-centrosymmetric Ge iodide perovskites show excellent nonlinear optical properties, with the highest reaching $0.53 \times \text{AGS}$ [for $(4\text{AMPY})\text{GeI}_4$]. The structural transformation from (100)- to (110)-oriented 2D layers can be successfully regulated by mixing Br with I, which works universally for the 2AMPY, 3AMPY, and 4AMPY cations. Our work on the new library of 2D Ge-based perovskites with structure–property insights opens a pathway for the rational design of nonlinear optical halide materials.

METHODS

Materials. GeO_2 (99.99%, BIDE), hydrobromic acid (40%, Macklin), hydroiodic acid ($\geq 47\%$, Macklin), hypophosphorous acid (50 wt % in H_2O , Aladdin), methylamine hydrochloride (98%, Macklin), 2-(aminomethyl)-pyridine (99.5%, Bidepharm), 3-(aminomethyl)-pyridine (99.9%, Bidepharm), 4-(aminomethyl)pyridine (99%, Bidepharm), and 4-(aminomethyl)piperidine (96%, Bidepharm) were purchased from commercial sources listed above and used without further purification.

Synthesis. $(2\text{AMPY})\text{GeBr}_4$, $(3\text{AMPY})\text{GeBr}_4$, $(4\text{AMPY})\text{GeBr}_4$, and $(4\text{AMPY})\text{GeI}_4$. For $(2\text{AMPY})\text{GeBr}_4$, 100 mg (1 mmol) of GeO_2 powder was dissolved in 8 mL of hydrobromic acid and 1.5 mL of a hypophosphorous acid solution by heating under stirring for 5 min at 126°C until the solution turned colorless. Then, 108 mg (1 mmol) of 2-(aminomethyl)pyridine (2AMPY) was added to the previous solution under heating at 126°C and stirring for 5 min. Colorless block-like crystals precipitated when the solution was cooled to room temperature. For $(3\text{AMPY})\text{GeBr}_4$, $(4\text{AMPY})\text{GeBr}_4$, and $(4\text{AMPY})\text{GeI}_4$, they follow the same route except the type of cation was changed to 3-(aminomethyl)pyridine (3AMPY), 4-(aminomethyl)pyridine (4AMPY), and 4-(aminomethyl)piperidine (4AMP), respectively, and then the light yellow plate-like crystals [$(3\text{AMPY})\text{GeBr}_4$ and $(4\text{AMPY})\text{GeBr}_4$] as well as colorless block-like crystals [$(4\text{AMPY})\text{GeI}_4$] were obtained during slow cooling to room temperature.

$(2\text{AMPY})\text{GeI}_4$, $(3\text{AMPY})\text{GeI}_4$, $(4\text{AMPY})\text{GeI}_4$, and $(4\text{AMPY})\text{GeI}_4$. For $(2\text{AMPY})\text{GeI}_4$, 100 mg (1 mmol) of GeO_2 powder was dissolved in 8 mL of hydroiodic acid and 1.5 mL of a hypophosphorous acid solution by heating under stirring for 10 min at 127°C until the solution turned bright yellow. Then, 108 mg (1 mmol) of 2AMPY was added to the solution described above under heating and stirring for an additional 5 min. Orange plate-like crystals precipitated during slow cooling. For $(3\text{AMPY})\text{GeI}_4$, $(4\text{AMPY})\text{GeI}_4$, and $(4\text{AMPY})\text{GeI}_4$, they follow the same route except the type of cation was changed to 3AMPY, 4AMPY, and 4AMP, respectively, and the orange plate-like crystals [$(3\text{AMPY})\text{GeI}_4$ and $(4\text{AMPY})\text{GeI}_4$], as well as yellow needle-like crystals [$(4\text{AMPY})\text{GeI}_4$], were obtained during slow cooling to room temperature.

$(3\text{AMPY})(\text{MA})\text{Ge}_2\text{I}_7$ and $(4\text{AMPY})(\text{MA})\text{Ge}_2\text{I}_7$. For $(3\text{AMPY})(\text{MA})\text{Ge}_2\text{I}_7$, 50 mg (0.5 mmol) of GeO_2 powder was dissolved in 7 mL of hydroiodic acid and 1.4 mL of the hypophosphorous acid solution by heating under stirring for 10 min at 127°C to form a bright yellow solution, and then 4 mL of deionized water was added. Next, 135.04 mg (2 mmol) of methylamine hydrochloride (MACl) and 64.8 mg (0.6 mmol) of 3AMPY were added directly to the solution described above under heating and stirring for 5 min. Afterward, the solution was cooled to room temperature, and orange plate-like crystals precipitated. For $(4\text{AMPY})(\text{MA})\text{Ge}_2\text{I}_7$, they follow the same route except that the type of cation was changed to 4AMPY, and the ratio was changed to 151.2 mg (1.4 mmol) of 4AMPY and 270.08 mg (4 mmol) of MACl. The orange plate-like crystals were obtained during slow cooling to room temperature.

$(2\text{AMPY})\text{GeBr}_x\text{I}_{4-x}$, $(3\text{AMPY})\text{GeBr}_x\text{I}_{4-x}$, and $(4\text{AMPY})\text{GeBr}_x\text{I}_{4-x}$. For $(2\text{AMPY})\text{GeBr}_x\text{I}_{4-x}$, we first prepared mixtures including various proportions of a mixed total acid (8 mL) by adding volumes of hydroiodic acid varying from 1 to 7 mL to hydrobromic acid. An amount of 50 mg (0.5 mmol) of GeO_2 powder was dissolved in each acid solution and 1.5 mL of the hypophosphorous acid solution by heating under stirring for 10 min at 127°C to form a pellucid solution. Then a total of 108 mg (1 mmol) of 2AMPY was added to each solution, and the resulting mixture was heated and stirred for an additional 5 min. Orange plate-like crystals precipitated when the solution was cooled to room temperature. For $(3\text{AMPY})\text{GeBr}_x\text{I}_{4-x}$, they follow the same route except that the type of cation was changed to 3AMPY and a volume of hydroiodic acid varying from 2 to 3 mL was added to hydrobromic acid on the basis of mixed total acid (8 mL). Orange plate-like crystals were obtained during slow cooling to room temperature. For $(4\text{AMPY})\text{GeBr}_x\text{I}_{4-x}$, they also follow the same route except that the type of cation was changed to 4AMPY and a

volume of hydroiodic acid varying from 1 to 4 mL was added to hydrobromic acid based on mixed total acid (8 mL). Orange plate-like crystals were obtained during slow cooling to room temperature.

Single-Crystal X-ray Diffraction. Single-crystal diffraction data were recorded using a Bruker D8 Venture diffractometer with Ga $K\alpha$ ($\lambda = 1.34139 \text{ \AA}$) radiation at 298 K [(2AMPY)GeBr₄ and (3AMPY)(MA)Ge₂I₄]. The rest of the compounds were collected using a Bruker D8 Venture diffractometer with Mo $K\alpha$ ($\lambda = 0.71073 \text{ \AA}$) radiation at 298 K. Data were collected and reduced using the Bruker APEX3 program for all compounds. The structures were determined by a direct method and refined with the OLEX2 program package based on F^2 with refinements of full-matrix least squares. All of the non-hydrogen atoms were refined with anisotropic thermal parameters.

Powder X-ray Diffraction (PXRD). Powder X-ray diffraction (PXRD) data were performed using a SmartLab X-ray diffractometer (Cu $K\alpha$ radiation; $\lambda = 1.54056 \text{ \AA}$) operating at 45 kV and 200 mA in the range of 5–50° to confirm the purity of each sample at room temperature.

Optical Absorption Spectroscopy. The optical absorption spectra were recorded on a Shimadzu UV-3600i Plus spectrophotometer with BaSO₄ as a standard with a wavelength range at 260–900 nm. The reflectance spectra were converted to absorption based on the Kubelka–Munk equation $\alpha/S = (1 - R)^2/(2R)^{-1}$, where α and S are the absorption and scattering coefficients, respectively, and R is the reflectance.

Steady-State Photoluminescence. Steady-state photoluminescence (PL) emission spectra of samples [(2AMPY)GeBr₄, (3AMPY)GeBr₄, and (4AMPY)GeBr₄] were recorded using the Edinburgh Instrument FLS-1000 spectrometer equipped with an excitation source of a xenon lamp (450 W) at 80 K. Temperature-dependent PL emission spectra of samples [(3AMPY)GeI₄ and (3AMPY)(MA)Ge₂I₇] were recorded by a NOVA spectrometer through the OLYMPUS confocal microscope excited by a MDL-III 405 nm laser.

Second-Harmonic Generation. The SHG signals of samples were measured by the Kurtz–Perry method⁵⁵ on a Q-switched Nd:YAG solid-state laser with two different lasers (1064 and 2050 nm) at room temperature. Crystals were ground and sieved into a particle size range (70–100 μm) based on KH₂PO₄ (KDP) as a reference and different particle size ranges (25–45, 45–62, 62–75, 75–109, 109–150, and 150–212 μm) based on AgGaS₂ (AGS) as a reference. KDP and AGS with the corresponding sizes were also used as the relevant comparison standard. The polarization-dependent SHG experiments were carried out by a conventional confocal microscope system at room temperature. The laser (Rainbow NOEM, 1550 nm) was focused on the crystals by a 5 \times objective (NA = 0.10). The reflected SHG signals were collected by an identical 5 \times objective, and the total signals were directly detected by a CCD camera or spectrometer coupled through an optical fiber. The polarizing filter was used to control the intensity and polarization direction of the laser.

Scanning Electron Microscopy (SEM). The morphology of the samples was characterized by scanning electron microscopy (JEOL JSM-7800F, operated at 5 kV), and the elemental composition of the samples was acquired by EDS coupled to SEM. The error ranges of quantitative analysis are less than $\pm 3\%$.

■ ASSOCIATED CONTENT

SI Supporting Information

The Supporting Information is available free of charge at <https://pubs.acs.org/doi/10.1021/acs.chemmater.3c00278>.

Experimental details, additional characterization, including PXRD, temperature-dependent PL spectra, UV–vis, SHG data, and crystallographic details (PDF)

Crystallographic data of 2238515 (CIF)

Crystallographic data of 2238516 (CIF)

Crystallographic data of 2238517 (CIF)

Crystallographic data of 2238518 (CIF)

Crystallographic data of 2238519 (CIF)

Crystallographic data of 2238520 (CIF)

Crystallographic data of 2238521 (CIF)

Crystallographic data of 2238522 (CIF)

Crystallographic data of 2238523 (CIF)

Crystallographic data of 2238524 (CIF)

Crystallographic data of 2238525 (CIF)

■ AUTHOR INFORMATION

Corresponding Authors

Pieremanuele Canepa – Department of Chemical and Biomolecular Engineering, National University of Singapore, 117585, Singapore; Department of Materials Science and Engineering, National University of Singapore, 117575, Singapore; orcid.org/0000-0002-5168-9253; Email: pcanepa@nus.edu.sg

Lingling Mao – Department of Chemistry, Southern University of Science and Technology, Shenzhen 518055, China; orcid.org/0000-0003-3166-8559; Email: maoll@sustech.edu.cn

Authors

Congcong Chen – Department of Chemistry, Southern University of Science and Technology, Shenzhen 518055, China; orcid.org/0000-0003-1016-8731

Xin Zhao – Key Laboratory of Optoelectronic Materials Chemistry and Physics, Fujian Institute of Research on the Structure of Matter, Chinese Academy of Sciences, Fuzhou, Fujian 350002, P. R. China

Yaping Gong – MOE Key Laboratory of Bioinorganic and Synthetic Chemistry, School of Chemistry, Sun Yat-Sen University, Guangzhou 510275, China

Yang Liu – Department of Chemistry, Southern University of Science and Technology, Shenzhen 518055, China; orcid.org/0000-0002-2189-4774

Zhongwei Chen – Department of Chemistry and Energy Institute, The Hong Kong University of Science and Technology, Kowloon 999077 Hong Kong (SAR), China

Luming Zhang – Department of Biology, School of Life Sciences, Southern University of Science and Technology, Shenzhen 518055, China

Jian Chen – Department of Chemistry, Southern University of Science and Technology, Shenzhen 518055, China

Zeyu Deng – Department of Chemical and Biomolecular Engineering, National University of Singapore, 117585, Singapore; orcid.org/0000-0003-0109-9367

Haipeng Lu – Department of Chemistry and Energy Institute, The Hong Kong University of Science and Technology, Kowloon 999077 Hong Kong (SAR), China; orcid.org/0000-0003-0252-3086

Min Luo – Key Laboratory of Optoelectronic Materials Chemistry and Physics, Fujian Institute of Research on the Structure of Matter, Chinese Academy of Sciences, Fuzhou, Fujian 350002, P. R. China; orcid.org/0000-0001-9062-8931

Complete contact information is available at:

<https://pubs.acs.org/doi/10.1021/acs.chemmater.3c00278>

Notes

The authors declare no competing financial interest.

ACKNOWLEDGMENTS

This work was supported by the National Natural Science Foundation of China (NSFC) under Grant 22275077, the Stable Support Plan Program of Shenzhen Natural Science Fund (Program Contract 20220814233319001), and the Startup Fund of SUSTech. Z.C. and H.L. are supported by the Research Grants Council of Hong Kong via the Early Career Scheme (ECS, 26300721) and the National Natural Science Foundation of China (Grant 22205186). The authors are grateful for the assistance of SUSTech Core Research Facilities.

REFERENCES

- (1) Jung, E. H.; Jeon, N. J.; Park, E. Y.; Moon, C. S.; Shin, T. J.; Yang, T.-Y.; Noh, J. H.; Seo, J. Efficient, stable and scalable perovskite solar cells using poly(3-hexylthiophene). *Nature* **2019**, *567*, 511–515.
- (2) Park, N.-G.; Zhu, K. Scalable fabrication and coating methods for perovskite solar cells and solar modules. *Nat. Rev. Mater.* **2020**, *5*, 333–350.
- (3) Wang, R.; Huang, T.; Xue, J.; Tong, J.; Zhu, K.; Yang, Y. Prospects for metal halide perovskite-based tandem solar cells. *Nat. Photonics* **2021**, *15*, 411–425.
- (4) Zhang, Y.; Park, N.-G. Quasi-Two-Dimensional Perovskite Solar Cells with Efficiency Exceeding 22%. *ACS Energy Lett.* **2022**, *7*, 757–765.
- (5) Tsai, H.; Liu, C.; Kinigstein, E.; Li, M.; Tretiak, S.; Cotlet, M.; Ma, X.; Zhang, X.; Nie, W. Critical Role of Organic Spacers for Bright 2D Layered Perovskites Light-Emitting Diodes. *Adv. Sci.* **2020**, *7*, 1903202.
- (6) Liu, X.-K.; Xu, W.; Bai, S.; Jin, Y.; Wang, J.; Friend, R. H.; Gao, F. Metal halide perovskites for light-emitting diodes. *Nat. Mater.* **2021**, *20*, 10–21.
- (7) Khan, R.; Chu, S.; Li, Z.; Ighodalo, K. O.; Chen, W.; Xiao, Z. High Radiance of Perovskite Light-Emitting Diodes Enabled by Perovskite Heterojunctions. *Adv. Fun. Mater.* **2022**, *32*, 2203650.
- (8) Zhang, Y.; Ma, Y.; Wang, Y.; Zhang, X.; Zuo, C.; Shen, L.; Ding, L. Lead-Free Perovskite Photodetectors: Progress, Challenges, and Opportunities. *Adv. Mater.* **2021**, *33*, 2006691.
- (9) Stoumpos, C. C.; Malliakas, C. D.; Peters, J. A.; Liu, Z.; Sebastian, M.; Im, J.; Chasapis, T. C.; Wibowo, A. C.; Chung, D. Y.; Freeman, A. J.; Wessels, B. W.; Kanatzidis, M. G. Crystal Growth of the Perovskite Semiconductor CsPbBr₃: A New Material for High-Energy Radiation Detection. *Cryst. Growth Des.* **2013**, *13*, 2722–2727.
- (10) Li, Z.; Liu, X.; Zuo, C.; Yang, W.; Fang, X. Supersaturation-Controlled Growth of Monolithically Integrated Lead-Free Halide Perovskite Single-Crystalline Thin Film for High-Sensitivity Photodetectors. *Adv. Mater.* **2021**, *33*, 2103010.
- (11) Qin, C.; Sandanayaka, A. S. D.; Zhao, C.; Matsushima, T.; Zhang, D.; Fujihara, T.; Adachi, C. Stable room-temperature continuous-wave lasing in quasi-2D perovskite films. *Nature* **2020**, *585*, 53–57.
- (12) Zhang, Q.; Shang, Q.; Su, R.; Do, T. T. H.; Xiong, Q. Halide Perovskite Semiconductor Lasers: Materials, Cavity Design, and Low Threshold. *Nano Lett.* **2021**, *21*, 1903–1914.
- (13) Zhu, H.; Fu, Y.; Meng, F.; Wu, X.; Gong, Z.; Ding, Q.; Gustafsson, M. V.; Trinh, M. T.; Jin, S.; Zhu, X. Y. Lead halide perovskite nanowire lasers with low lasing thresholds and high quality factors. *Nat. Mater.* **2015**, *14*, 636–642.
- (14) Stoumpos, C. C.; Kanatzidis, M. G. The Renaissance of Halide Perovskites and Their Evolution as Emerging Semiconductors. *Acc. Chem. Res.* **2015**, *48*, 2791–2802.
- (15) Jena, A. K.; Kulkarni, A.; Miyasaka, T. Halide Perovskite Photovoltaics: Background, Status, and Future Prospects. *Chem. Rev.* **2019**, *119*, 3036–3103.
- (16) Saparov, B.; Mitzi, D. B. Organic–Inorganic Perovskites: Structural Versatility for Functional Materials Design. *Chem. Rev.* **2016**, *116*, 4558–4596.
- (17) Cheng, L.; Liu, Z.; Li, S.; Zhai, Y.; Wang, X.; Qiao, Z.; Xu, Q.; Meng, K.; Zhu, Z.; Chen, G. Highly Thermostable and Efficient Formamidinium-Based Low-Dimensional Perovskite Solar Cells. *Angew. Chem., Int. Ed.* **2021**, *60*, 856–864.
- (18) Mao, L.; Wu, Y.; Stoumpos, C. C.; Wasielewski, M. R.; Kanatzidis, M. G. White-Light Emission and Structural Distortion in New Corrugated Two-Dimensional Lead Bromide Perovskites. *J. Am. Chem. Soc.* **2017**, *139*, 5210–5215.
- (19) Stoumpos, C. C.; Cao, D. H.; Clark, D. J.; Young, J.; Rondinelli, J. M.; Jang, J. I.; Hupp, J. T.; Kanatzidis, M. G. Ruddlesden–Popper Hybrid Lead Iodide Perovskite 2D Homologous Semiconductors. *Chem. Mater.* **2016**, *28*, 2852–2867.
- (20) Pareja-Rivera, C.; Morán-Muñoz, J. A.; Gómora-Figueroa, A. P.; Jancik, V.; Vargas, B.; Rodríguez-Hernández, J.; Solís-Ibarra, D. Optimizing Broadband Emission in 2D Halide Perovskites. *Chem. Mater.* **2022**, *34*, 9344–9349.
- (21) Fu, Y.; Jiang, X.; Li, X.; Traore, B.; Spanopoulos, I.; Katan, C.; Even, J.; Kanatzidis, M. G.; Harel, E. Cation Engineering in Two-Dimensional Ruddlesden–Popper Lead Iodide Perovskites with Mixed Large A-Site Cations in the Cages. *J. Am. Chem. Soc.* **2020**, *142*, 4008–4021.
- (22) Mao, L.; Ke, W.; Pedesseau, L.; Wu, Y.; Katan, C.; Even, J.; Wasielewski, M. R.; Stoumpos, C. C.; Kanatzidis, M. G. Hybrid Dion–Jacobson 2D Lead Iodide Perovskites. *J. Am. Chem. Soc.* **2018**, *140*, 3775–3783.
- (23) Li, X.; Ke, W.; Traoré, B.; Guo, P.; Hadar, I.; Kepenekian, M.; Even, J.; Katan, C.; Stoumpos, C. C.; Schaller, R. D.; Kanatzidis, M. G. Two-Dimensional Dion–Jacobson Hybrid Lead Iodide Perovskites with Aromatic Diammonium Cations. *J. Am. Chem. Soc.* **2019**, *141*, 12880–12890.
- (24) Gao, L.; Li, X.; Traoré, B.; Zhang, Y.; Fang, J.; Han, Y.; Even, J.; Katan, C.; Zhao, K.; Liu, S.; Kanatzidis, M. G. *m*-Phenylenediammonium as a New Spacer for Dion–Jacobson Two-Dimensional Perovskites. *J. Am. Chem. Soc.* **2021**, *143*, 12063–12073.
- (25) Mao, L.; Guo, P.; Kepenekian, M.; Spanopoulos, I.; He, Y.; Katan, C.; Even, J.; Schaller, R. D.; Seshadri, R.; Stoumpos, C. C.; Kanatzidis, M. G. Organic Cation Alloying on Intralayer A and Interlayer A' sites in 2D Hybrid Dion–Jacobson Lead Bromide Perovskites (A')(A)Pb₂Br₇. *J. Am. Chem. Soc.* **2020**, *142*, 8342–8351.
- (26) Fu, D.; Hou, Z.; He, Y.; Wu, H.; Wu, S.; Zhang, Y.; Niu, G.; Zhang, X.-M. Formamidinium Perovskitizers and Aromatic Spacers Synergistically Building Bilayer Dion–Jacobson Perovskite Photoelectric Bulk Crystals. *ACS Appl. Mater. Interfaces* **2022**, *14*, 11690–11698.
- (27) Soe, C. M. M.; Stoumpos, C. C.; Kepenekian, M.; Traoré, B.; Tsai, H.; Nie, W.; Wang, B.; Katan, C.; Seshadri, R.; Mohite, A. D.; Even, J.; Marks, T. J.; Kanatzidis, M. G. New Type of 2D Perovskites with Alternating Cations in the Interlayer Space, (C(NH₂)₃)-(CH₃NH₃)_nPb_nI_{3n+1}: Structure, Properties, and Photovoltaic Performance. *J. Am. Chem. Soc.* **2017**, *139*, 16297–16309.
- (28) Mao, L.; Morgan, E. E.; Li, A.; Kennard, R. M.; Hong, M. J.; Liu, Y.; Dahllman, C. J.; Labram, J. G.; Chabinc, M. L.; Seshadri, R. Layered Hybrid Lead Iodide Perovskites with Short Interlayer Distances. *ACS Energy Lett.* **2022**, *7*, 2801–2806.
- (29) Li, W.; Sidhik, S.; Traore, B.; Asadpour, R.; Hou, J.; Zhang, H.; Fehr, A.; Essman, J.; Wang, Y.; Hoffman, J. M.; Spanopoulos, I.; Crochet, J. J.; Tsai, E.; Strzalka, J.; Katan, C.; Alam, M. A.; Kanatzidis, M. G.; Even, J.; Blancon, J.-C.; Mohite, A. D. Light-activated interlayer contraction in two-dimensional perovskites for high-efficiency solar cells. *Nat. Nanotechnol.* **2022**, *17*, 45–52.
- (30) Ghosh, D.; Acharya, D.; Pedesseau, L.; Katan, C.; Even, J.; Tretiak, S.; Neukirch, A. J. Charge carrier dynamics in two-dimensional hybrid perovskites: Dion–Jacobson vs. Ruddlesden–Popper phases. *J. Mater. Chem. A* **2020**, *8*, 22009–22022.
- (31) Stoumpos, C. C.; Frazer, L.; Clark, D. J.; Kim, Y. S.; Rhim, S. H.; Freeman, A. J.; Ketterson, J. B.; Jang, J. I.; Kanatzidis, M. G. Hybrid Germanium Iodide Perovskite Semiconductors: Active Lone Pairs, Structural Distortions, Direct and Indirect Energy Gaps, and

Strong Nonlinear Optical Properties. *J. Am. Chem. Soc.* **2015**, *137*, 6804–6819.

(32) Liu, Y.; Gong, Y.-P.; Geng, S.; Feng, M.-L.; Manidakis, D.; Deng, Z.; Stoumpos, C. C.; Canepa, P.; Xiao, Z.; Zhang, W.-X.; Mao, L. Hybrid Germanium Bromide Perovskites with Tunable Second Harmonic Generation. *Angew. Chem., Int. Ed.* **2022**, *61*, e202208875.

(33) Lü, X.; Stoumpos, C.; Hu, Q.; Ma, X.; Zhang, D.; Guo, S.; Hoffman, J.; Bu, K.; Guo, X.; Wang, Y.; Ji, C.; Chen, H.; Xu, H.; Jia, Q.; Yang, W.; Kanatzidis, M. G.; Mao, H.-K. Regulating off-centering distortion maximizes photoluminescence in halide perovskites. *Nat. Sci. Rev.* **2021**, *8*, nwa288.

(34) Mitzi, D. B. Synthesis, Crystal Structure, and Optical and Thermal Properties of $(C_4H_9NH_3)_2MI_4$ ($M = Ge, Sn, Pb$). *Chem. Mater.* **1996**, *8*, 791–800.

(35) Cheng, P.; Wu, T.; Zhang, J.; Li, Y.; Liu, J.; Jiang, L.; Mao, X.; Lu, R.-F.; Deng, W.-Q.; Han, K. $(C_6H_5C_2H_4NH_3)_2GeI_4$: A Layered Two-Dimensional Perovskite with Potential for Photovoltaic Applications. *J. Phys. Chem. Lett.* **2017**, *8*, 4402–4406.

(36) Li, X.; Guan, Y.; Li, X.; Fu, Y. Stereochemically Active Lone Pairs and Nonlinear Optical Properties of Two-Dimensional Multi-layered Tin and Germanium Iodide Perovskites. *J. Am. Chem. Soc.* **2022**, *144*, 18030–18042.

(37) Chiara, R.; Morana, M.; Boiocchi, M.; Coduri, M.; Striccoli, M.; Fracassi, F.; Listorti, A.; Mahata, A.; Quadrelli, P.; Gaboardi, M.; Milanese, C.; Bindi, L.; De Angelis, F.; Malavasi, L. Role of spacer cations and structural distortion in two-dimensional germanium halide perovskites. *J. Mater. Chem. C* **2021**, *9*, 9899–9906.

(38) Chen, C.; Morgan, E. E.; Liu, Y.; Chen, J.; Seshadri, R.; Mao, L. Breathing” organic cation to stabilize multiple structures in low-dimensional Ge-, Sn-, and Pb-based hybrid iodide perovskites. *Inorg. Chem. Front.* **2022**, *9*, 4892–4898.

(39) Momma, K.; Izumi, F. VESTA 3 for three-dimensional visualization of crystal, volumetric and morphology data. *J. Appl. Crystallogr.* **2011**, *44*, 1272–1276.

(40) Robinson, K.; Gibbs, G. V.; Ribbe, P. H. Quadratic Elongation: A Quantitative Measure of Distortion in Coordination Polyhedra. *Science* **1971**, *172*, 567–570.

(41) Mao, L.; Tsai, H.; Nie, W.; Ma, L.; Im, J.; Stoumpos, C. C.; Malliakas, C. D.; Hao, F.; Wasielewski, M. R.; Mohite, A. D.; Kanatzidis, M. G. Role of Organic Counterion in Lead- and Tin-Based Two-Dimensional Semiconducting Iodide Perovskites and Application in Planar Solar Cells. *Chem. Mater.* **2016**, *28*, 7781–7792.

(42) Kortüm, G.; Braun, W.; Herzog, G. Principles and Techniques of Diffuse-Reflectance Spectroscopy. *Angew. Chem., Int. Ed.* **1963**, *2*, 333–341.

(43) Takagahara, T. Electron–phonon interactions in semiconductor nanocrystals. *J. Lumin.* **1996**, *70*, 129–143.

(44) Wehrenfennig, C.; Liu, M.; Snaith, H. J.; Johnston, M. B.; Herz, L. M. Homogeneous Emission Line Broadening in the Organo Lead Halide Perovskite $CH_3NH_3PbI_{3-x}Cl_x$. *J. Phys. Chem. Lett.* **2014**, *5*, 1300–1306.

(45) Spanopoulos, I.; Hadar, I.; Ke, W.; Guo, P.; Mozur, E. M.; Morgan, E.; Wang, S.; Zheng, D.; Padgaonkar, S.; Manjunatha Reddy, G. N.; Weiss, E. A.; Hersam, M. C.; Seshadri, R.; Schaller, R. D.; Kanatzidis, M. G. Tunable Broad Light Emission from 3D “Hollow” Bromide Perovskites through Defect Engineering. *J. Am. Chem. Soc.* **2021**, *143*, 7069–7080.

(46) Mao, L.; Wu, Y.; Stoumpos, C. C.; Traore, B.; Katan, C.; Even, J.; Wasielewski, M. R.; Kanatzidis, M. G. Tunable White-Light Emission in Single-Cation-Templated Three-Layered 2D Perovskites $(CH_3CH_2NH_3)_4Pb_3Br_{10-x}Cl_x$. *J. Am. Chem. Soc.* **2017**, *139*, 11956–11963.

(47) Wang, S.; Yao, Y.; Wu, Z.; Peng, Y.; Li, L.; Luo, J. Realization of “warm” white light via halide substitution in polar two-dimensional hybrid perovskites $(2\text{meptH}_2)\text{PbCl}_x\text{Br}_{4-x}$. *J. Mater. Chem. C* **2018**, *6*, 12267–12272.

(48) Shen, Y. R. *Principles of nonlinear optics*; Wiley-Interscience: New York, 1984.

(49) Park, I.-H.; Zhang, Q.; Kwon, K. C.; Zhu, Z.; Yu, W.; Leng, K.; Giovanni, D.; Choi, H. S.; Abdelwahab, I.; Xu, Q.-H.; Sum, T. C.; Loh, K. P. Ferroelectricity and Rashba Effect in a Two-Dimensional Dion-Jacobson Hybrid Organic–Inorganic Perovskite. *J. Am. Chem. Soc.* **2019**, *141*, 15972–15976.

(50) Yu, Z.; Cao, S.; Zhao, Y.; Guo, Y.; Dong, M.; Fu, Y.; Zhao, J.; Yang, J.; Jiang, L.; Wu, Y. Chiral Lead-Free Double Perovskite Single-Crystalline Microwire Arrays for Anisotropic Second-Harmonic Generation. *ACS Appl. Mater. Interfaces* **2022**, *14*, 39451–39458.

(51) Zheng, Y.; Han, X.; Cheng, P.; Jia, X.; Xu, J.; Bu, X.-H. Induction of Chiral Hybrid Metal Halides from Achiral Building Blocks. *J. Am. Chem. Soc.* **2022**, *144*, 16471–16479.

(52) Guo, Z.; Li, J.; Liang, J.; Wang, C.; Zhu, X.; He, T. Regulating Optical Activity and Anisotropic Second-Harmonic Generation in Zero-Dimensional Hybrid Copper Halides. *Nano Lett.* **2022**, *22*, 846–852.

(53) Kasel, T. W.; Deng, Z.; Mroz, A. M.; Hendon, C. H.; Butler, K. T.; Canepa, P. Metal-free perovskites for non linear optical materials. *Chem. Sci.* **2019**, *10*, 8187–8194.

(54) Dovesi, R.; Saunders, V. R.; Roetti, C. R.; Orlando, R.; Zicovich-Wilson, C. M.; Pascale, F.; Civaleri, B.; Doll, K.; Harrison, N. M.; Bush, I. J.; D’Arco, P.; Llunell, M.; Caus’ a, M.; Nöel, Y.; Maschio, L.; Erba, A.; Rerat, M.; Casassa, S. *CRYSTAL17 User’s Manual*; University of Torino: Torino, Italy, 2017.

(55) Kurtz, S. K.; Perry, T. T. A Powder Technique for the Evaluation of Nonlinear Optical Materials. *J. Appl. Phys.* **1968**, *39*, 3798–3813.